2014

Optimization Of A Heat Pump For Satellite Cooling

Ian Bell
University of Liège, Liège, Belgium, ian.bell@ulg.ac.be

Vincent Lemort
University of Liège, Liège, Belgium, vincent.lemort@ulg.ac.be

Optimization Of A Heat Pump For Satellite Cooling

Ian BELL[1*], Vincent LEMORT[1]

[1] Energy Systems Research Unit,
University of Liège, Liège, Belgium
ian.bell@ulg.ac.be, vincent.lemort@ulg.ac.be

* Corresponding Author

ABSTRACT

In recent years the heat fluxes that must be removed from terrestrial electrical systems have been steadily increasing. The same increase in electrical component heat flux can also be seen in satellite and aerospace applications. As a result, it has proven necessary to develop heat pump systems that can operate in low-gravity environments with high reliability and efficiency to cool electrical components in the satellite. It is currently common practice to use heat pipes to conduct the heat generated by the electrical components to the radiators of the satellite, but tomorrow's electrical components will have heat fluxes high enough to make this system no longer feasible.

The heat pump system considered here is a conventional four-component heat pump (compressor, condenser, expansion valve, evaporator) that uses an oil-free scroll compressor in place of the oil-lubricated compressor that is more often employed for terrestrial applications. There are a number of other unique features to this system, including the fact that all the heat rejection occurs through radiative heat transfer and the heat load is fixed (rather than being a function of source and sink temperatures). These unique features result in a system behavior that is quite different than conventional air-to-air heat pumps.

The first part of this study considers the fluid selection, as choosing the best working fluid is critical for the overall performance and environmental safety of the system. This study then delves into the detailed performance analysis of the oil-free scroll compressors that are envisaged to be used in this system. Finally, the entire operating envelope of the heat pump system is considered, including variations in electrical load and seasonal variations in the radiative environmental temperature.

1. INTRODUCTION

Satellites are deployed into near earth orbit in order to provide a platform for a wide range of missions, including telecommunications systems, surveillance systems, and astronomical systems, amongst others. For terrestrial electronics systems, the last few decades have brought with them a large increase in electrical component power density. Aerospace applications have seen a similar increase in electrical power density of their electrical payloads, which results in a commensurate need in cooling for the electronic components.

In the past, the cooling of the components of satellites was achieved through the use of heat pipes connecting the electrical components and large radiators. As the electrical cooling demands have increased, the available area for the radiator exposed surface area has not increased at the same pace. Therefore, to reject more heat for a given radiator area, the surface temperature of the radiator must increase.

If the desired radiator surface temperature is above the working temperature of the electrical components to be cooled, it is necessary to employ active cooling through the use of a heat pump to boost the temperature of a working fluid above the desired radiator surface temperature. Through condensation of the working fluid, the heat can be rejected through the radiator.

The heat pump systems required for aerospace applications share many commonalities with those of terrestrial applications. In the simplest case, both terrestrial and aerospace heat pump units are composed of the conventional four-component system - compressor, condenser, expansion device and evaporator.

In some important ways, design and optimization of heat pumps for aerospace applications differs from that of terrestrial applications. Three of the most important considerations are:

- Satellites must be delivered to near-earth-orbit by rocket engines, which is very expensive (USD $25,000/kg [1]).
- The satellite will operate in a low-gravity environment, making oil-refrigerant separation difficult
- There is no possibility of servicing the system during its lifetime.

2. SYSTEM MODELING

2.1 Overview

The heat pump of a satellite cooling system is composed of four components as seen in Figure 1(a). A compressor compresses the working fluid from evaporating to condensing pressure, the working fluid is condensed in the radiatively-cooled condenser, the working fluid is expanded in the expansion valve, and then the cool working fluid boils in the evaporator which cools the electrical load. One of the particularities of this system is that the capacity is directly fixed by the electrical load in the heaters, rather than being partially governed by the source temperature. Here the temperature of the electrical elements coupled with the evaporator are obtained as an output of the simulation. In this case, both heat exchangers employ microchannel heat exchangers for weight considerations.

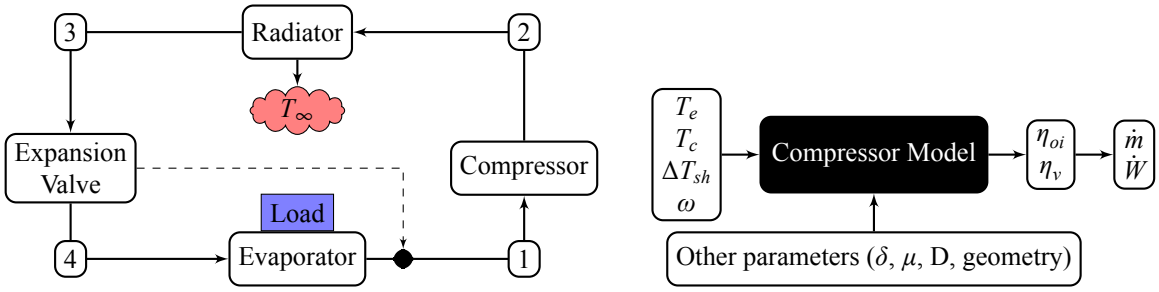

(a) System schematic (b) Block diagram for compressor model

Figure 1: System and Compressor schematics

2.2 Compressor

Once the working fluid has been selected, the performance of the compressor can be correlated with the boundary conditions of the compressor, namely the inlet and outlet saturation temperatures, as seen in Figure 1(b). The form of the model for the compressor employed could be either a very detailed mechanistic simulation like PDSim described below, or for computational efficiency reasons, a polynomial like equation. In this paper, both types of compressor models are used.

2.3 Expansion valve

In the case, the expansion valve is taken to have idealized behavior; the expansion valve is assumed to be always able to maintain the desired superheat at the outlet of the evaporator for all operating conditions.

2.4 Radiator

The radiator in this case is taken to be a square with length per side of L_{rad} as seen in Figure 2(a). There are then a given number of passes N_{pass}, which yields a width of radiator per pass of $w_{pass} = L_{rad}/N_{pass}$. The total length of the circuit is equal to $L_{circuit} = N_{pass}L_{rad}$.

[1] http://earsc.org/news/isro-to-launch-french-satellite-in-2012

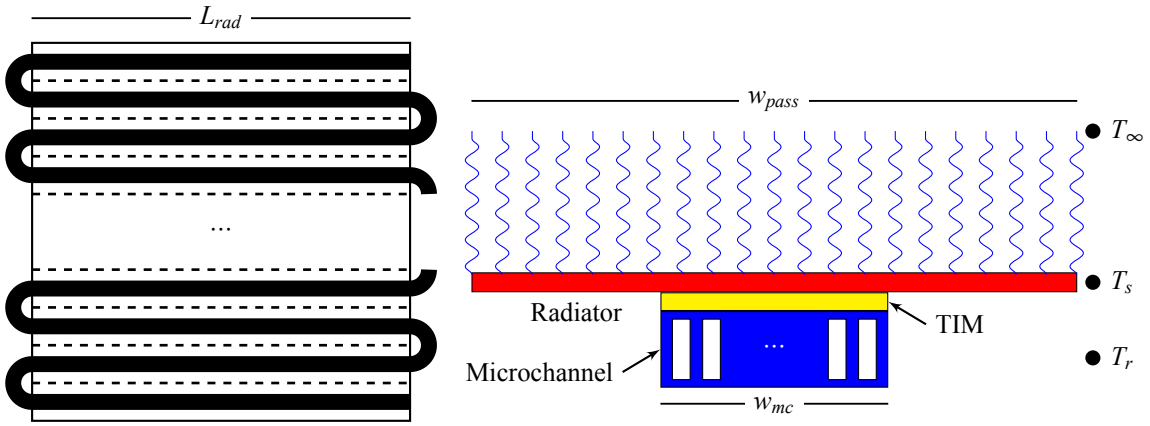

(a) Overall schematic of radiator (b) Radiator pass cross-section

Figure 2: Radiator schematic

The pass is formed of a microchannel condenser channel connected to a radiator panel through a thermal interface material (TIM) as seen in Figure 2(b). The thermal interface material causes a significant thermal gradient due to its relatively poor thermal conductance.

The local surface temperature can be obtained from the energy balance at the radiator surface which is at a temperature of T_s. Here we assume that the radiator surface has infinitely high thermal conductance resulting in no spreading losses. Thus the energy balance can be given by

$$-q' = \varepsilon\sigma(T_s^4 - T_\infty^4)w_{pass} = \frac{T_r - T_s}{R_{total}}w_{mc} \tag{1}$$

where q' is the heat transfer per unit length in W/m, T_s is the surface temperature in K, T_∞ is the ambient temperature in K, T_r is the working fluid temperature in K, R_{total} is the combined thermal resistance of the TIM and microchannel in $m^2 \cdot K \cdot W^{-1}$. This equation must be solved numerically for T_s. It is known that T_s is between T_∞ and T_r, so a bounded solver like Brent's method can be used to solve, guaranteeing a solution. The total thermal resistance between the surface temperature and the refrigerant temperature is given by

$$R_{total} = R_{conv}w_{mc} + R_{TIM}. \tag{2}$$

The thermal interface resistance R_{TIM} is given by the thermal interface material selected, which in this case is an aerospace-grade thermal interface material (TIM)[2] compatible with the vacuum of interstellar space. This TIM has a thermal impedance of 1.03 $cm^2 \cdot K \cdot W^{-1}$. The "convective" thermal resistance is given by

$$R_{conv} = (\eta_0 \alpha w_{mc})^{-1} \tag{3}$$

where α is the heat transfer coefficient in the channel in $W \cdot m^{-2} \cdot K^{-1}$, η_0 is the overall surface effectiveness, and w_{mc} is the total width of the microchannel condenser in m. The surface effectiveness is based on the heat transfer coefficient in the channel and the microchannel condenser dimensions. The heat transfer correlation is selected based on the local phase of the fluid:

Table 1: Correlations used in microchannel condenser

	Heat Transfer	Pressure Drop
Single-Phase	Gnielinski (1975)	Churchill (1977)
Two-Phase	Shah (1979)	Kim & Mudawar (2012)

[2]Laird Technologies TPLI 210

Each pass is subdivided into a number of elements, and in each element, the inlet state is used to predict the surface temperature and the heat transfer rate per unit length q' for the element as well as the pressure gradient in the element. The outlet enthalpy and pressure of the element can be obtained from

$$h_o = h_i - \frac{q'l}{\dot{m}} \quad \& \quad p_o = p_i + \frac{dp}{dz}l \tag{4}$$

where l is the length (in m) of an element of the circuit. The total pressure drop is obtained as the summation of the pressure drops from each element, and the heat transfer rate is obtained as the summation of the heat transfer in each element. The dimensions of the microchannel heat exchanger are given in Table 2. These dimensions correspond to a ratio w_{mc}/w_{pass} of approximately 4:1.

Table 2: Microchannel condenser dimension

Parameter	Value	Parameter	Value
L_{rad}	5 m	$N_{channel}$	10
w_i	3.1 mm	h_i	12.4 mm
w_{mc}	60 mm		

2.5 Evaporator

The evaporator considered in this analysis is a best-case evaporator with a uniform heat load along the entire length of the evaporator. The evaporator is given a fixed heat transfer rate of 12 kW. In reality the load profile in the evaporator is much more uneven, with a mixture of different maximum unit temperatures and heat fluxes. The surface temperature can be obtained directly from the heat flux applied by the electrical units.

$$T_s = q'' R_{total} + T_r. \tag{5}$$

The pressure drop in the evaporator also tends to decrease the refrigerant temperature along the length of the evaporator in the flow direction.

As in the radiator, the evaporator is subdivided into a number of elements, and in each element, the inlet state of the element is used to determine the heat transfer coefficient and pressure gradient for the element. The correlations used are:

Table 3: Correlations used in microchannel evaporators

	Heat Transfer	Pressure Drop
Single-Phase	Gnielinski (1975)	Churchill (1977)
Two-Phase	Bertsch et al. (2009)	Kim & Mudawar (2013)

The evaporator is formed of 10 channels, each 3.1 mm in width and 6.2 mm in height.

In current high-power electrical components, heat fluxes of 100 W·cm^{-2} are typical (Herwig, 2013); this flux is put through a 20x thermal spreader to reduce the heat flux at the microchannel evaporator to 5 W·cm^{-2}. The same TIM material is selected for the junction between the microchannel and the electrical units. The thermal impedance is 1.03 cm^2·K·W^{-1}, which will result in a temperature rise over the TIM of 5.15 K. The thermal resistance from the flow boiling and surface efficiency in the evaporator will contribute to an additional increase in the unit temperature.

2.6 Integration

Finally the entire system analysis can be carried out by solving a 3 input / 3 output system model. The inputs are the inlet pressure to the compressor, the outlet pressure of the compressor and the inlet pressure to the evaporator. The constraints are that the subcooling and superheating are both fixed at 5 K. The residual functions to be driven to zero by the nonlinear system of equations solver are

- Capacity of the evaporator must be equal to electrical load. ($r_0 = \dot{m}(h_1 - h_4) - \dot{Q}_{load}$)

- Actual subcooling[3] must equal target subcooling ($r_1 = \Delta T_{sc} - \Delta T_{sc,target}$)
- Pressure drop of the evaporator must equal difference in pressures over evaporator ($r_2 = p_{e,i} - p_{e,o} - \Delta p_e$)

Newton's method is used to solve the system of non-linear equations.

3. WORKING FLUID SELECTION

So far, the analysis has been working fluid agnostic, but not all working fluids are well suited to this application. As a first cut, the fluid must be able to condense and evaporate between the triple point and the critical point. Furthermore, the fluid must have acceptable environmental characteristics (toxicity and flammability) which will be described below.

Based on preliminary analysis and the constraints given above, the evaporating and condensing saturated temperatures can be estimated. This analysis predicts that the evaporating and condensing temperatures should be approximately 40°C and 90°C respectively. In order to carry out the first cut of fluid selection, the entire fluid library of CoolProp 4.2 is employed, which includes 114 pure and pseudo-pure fluids (Bell et al., 2014). The first thermodynamic filtering is to keep all the fluids for which $T_{\text{triple}} < 40°\text{C}$ and $T_{\text{crit}} > 90°\text{C}$; when the first filtering is applied, 78 fluids remain.

The next step is to consider flammability, toxicity and environmental compatibility. For this application, very flammable and very toxic fluids are deemed not acceptable. Based on the known flammability of certain classes of fluids (alkanes, alkenes, alkynes, fatty-acid methyl esters, alcohols) and/or toxicity (ASHRAE Standard 34 classes B1 and B2), the list of candidate fluids can be reduced to 33.

The next step is to consider that all the fluids could have systems designed for them that would allow for them to yield the same evaporating and condensing temperatures. Table 4 summarizes the performance of the cycles based on the assumption of equivalent isentropic efficiencies of 0.6 for all fluids. As seen in Figure 3, there are a family of fluids that could be used - the general trend is that displacement and COP increase with the critical temperature for the working conditions selected. A large COP and a small (but not too small) displacement are desired, and a good tradeoff between efficiency and displacement can be found with the working fluid R152A.

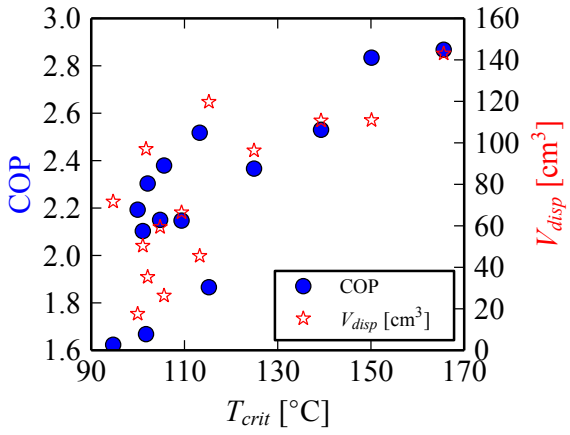

Figure 3: Displacement and COP versus critical temperature

Name	T_{triple} °C	T_{crit} °C	V_{disp} cm^3	COP -
H_2S	-85.4	100.0	17.6	2.2
OCS[a]	-138.8	105.6	26.3	2.4
R161	-143.1	102.1	35.3	2.3
R152A	-118.6	113.3	45.5	2.5
R134a	-103.3	101.1	50.4	2.1
HFE143m	-33.1	104.8	59.4	2.2
R1234ze(E)	-104.5	109.4	66.5	2.1
R1234yf	-53.1	94.7	71.7	1.6
R236FA	-93.5	124.9	96.3	2.4
R227EA	-126.8	101.8	97.0	1.7
R236EA	-103.1	139.3	110.8	2.5
R1234ze(Z)	-0.1	150.1	110.9	2.8

a: Carbonyl Sulfide

Table 4: Candidate working fluids

4. COMPRESSOR ANALYSIS

The compressor style selected for this aerospace heat pump application is a scroll compressor. This style of compressor is a well-proven technology for terrestrial air conditioning and heat pump applications. The scroll compressor is characterized by having few moving parts, no valves, and generally high performance over a wide range of operating

[3] A pseudo subcooling $\tilde{\Delta}T_{sc} = -xh_{fg}/c'_p$ is used if the outlet of the radiator is two-phase at an intermediate point in iteration.

conditions. In addition, oil-free scroll compressors are already available on the market for terrestrial heat pumps, which will reduce the new engineering required for this application.

The open-source mechanistic code **P**ositive **D**isplacement **Sim**ulation (PDSim) has been developed by the authors and is used to simulate the compressor performance. The source code of the simulation framework used to generate the compressor results in this paper is available as a digital appendix to this paper at ORBI[4].

Selection of the dimensions and other parameters of the compressor are highly dependent on the working fluid selected for the system. Furthermore, due to the zero-gravity application, it has been decided use a non-lubricated machine; this decision will have significant consequences on the machine's performance as the leakage gap widths must be properly selected to avoid scroll/scroll contact. From discussions with experienced engineers, it seems gap widths of 20 μm are about the best that could be achieved for oil-free scroll machines.

The source code, installer for PDSim, and configuration files required for PDSim can be obtained from ORBI. The most important compressor design parameters are summarized in Table 5. The other input parameters are given in the PDSim input file.

Table 5: Inputs for PDSim

Parameter	Value
Displacement volume [cm^3/rev]	45
Built-in volume ratio [-]	2.7
Leakage gap widths [μm]	20
Motor+Drive efficiency [%]	95
Refrigerant	R152A

4.1 Compressor Parametric Study

Figure 4 gives the results from the simulation of the non-lubricated compressor for this heat pump system. The evaporation saturation temperatures, condensing saturation temperature and rotational frequencies were linearly varied in the following ranges:

- T_e: suction saturation temperature (based on the inlet pressure to the compressor) in the range 30°C to 50°C
- T_c: discharge saturation temperature (based on the outlet pressure from the compressor) in the range 70°C to 90°C
- f: rotational frequency in the range 30 Hz to 80 Hz

From these ninety data points it can be seen that the volumetric efficiency is a very strong function of the rotational speed, and a weak function of the saturated temperatures. The volumetric efficiency increases as the difference $T_c - T_e$ decreases. A somewhat similar trend can be seen for the overall isentropic efficiency. In general, the isentropic efficiency increases monotonically with the rotational speed. There is a ridge in the overall isentropic efficiency surface for a given rotational speed. The optimal overall isentropic efficiency ridge is obtained for a temperature difference $T_c - T_e$ of approximately 45 K. This optimal efficiency ridge represents the points for which the built-in volume ratio best matches the imposed pressure ratio.

[4]http://orbi.ulg.ac.be/handle/2268/164968

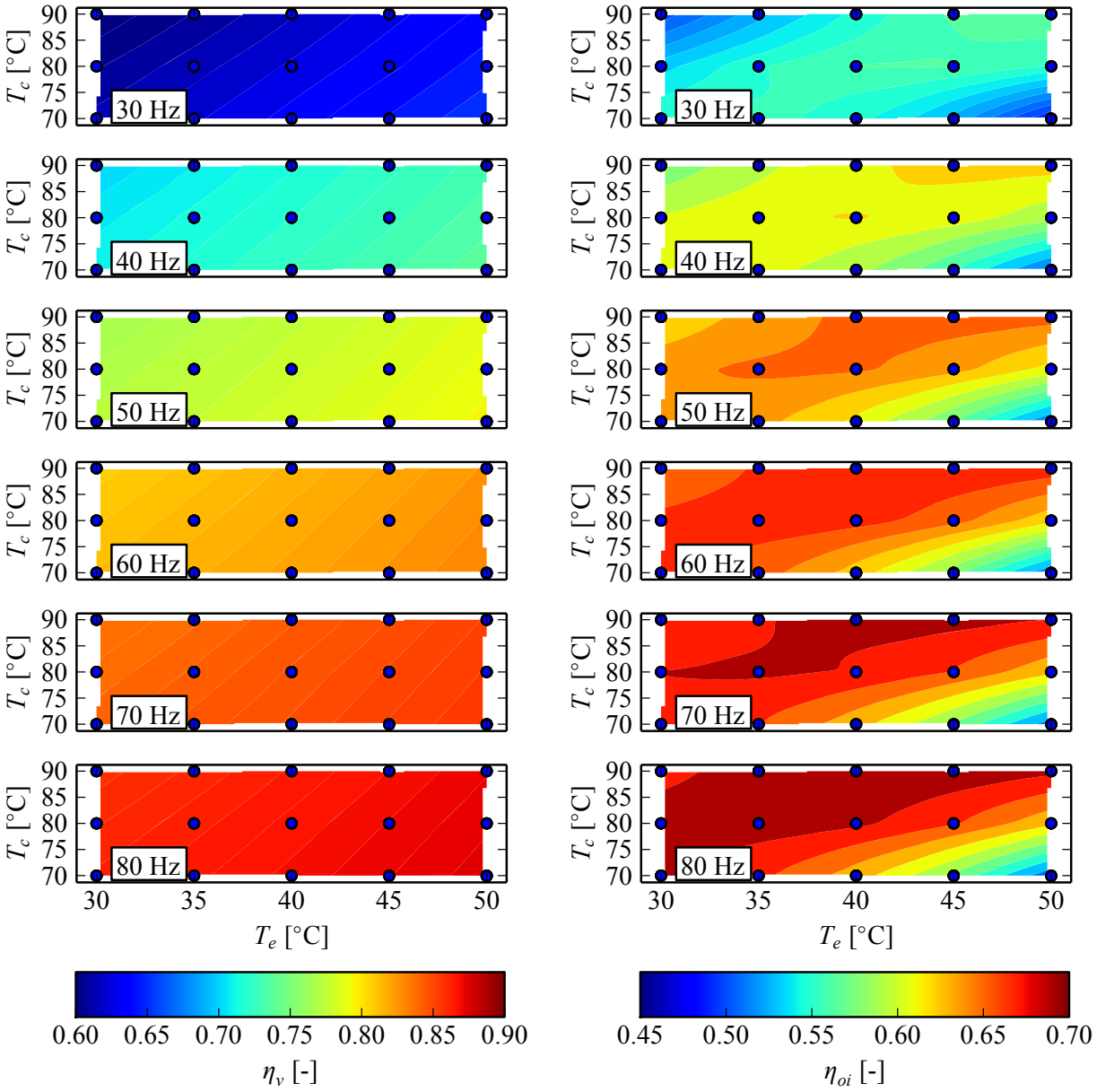

(a) Volumetric efficiency

(b) Overall isentropic efficiency

Figure 4: Results of the compressor simulation in PDSim

4.2 Compressor Map

Over the ninety data points presented above, the mean elapsed time for one simulation run was 257 seconds, or a little over 4 minutes. While this computational speed is excellent when considering the capabilities of the simulation code, it is much too slow for use the the integrated cycle model. Therefore it is necessary to either obtain a correlation for compressor performance or to carry out a multi-dimensional interpolation. In this case it was determined to employ a correlative method where the overall isentropic and volumetric efficiencies are fit as a function of reduced rotational speed and reduced saturation temperatures. The correlations obtained yield high-fidelity predictions of the compressor performance over the range of data points used to fit them. Figure 5 and the equations beside it show the form of the correlations used. The average absolute error of the volumetric and overall isentropic efficiency correlations are 0.66% and 1.07% respectively. The coefficients B_i and C_i are given in Table 6.

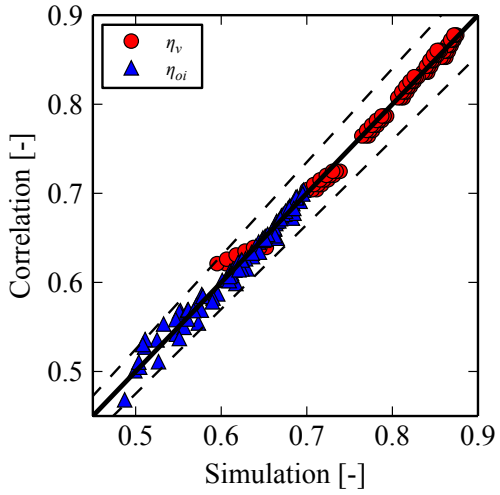

Figure 5: Accuracy of correlations used for the compressor model (dashed lines show ±5%)

$$\eta_v = (B_0 T_{er} + B_1 T_{er}^2 + B_2 T_{er}^3)(\omega_r^{B_3} + B_4 \omega_r)$$

$$\eta_{oi} = C_0 T_{cr} + C_1 \omega_r + C_2 T_{cr}^2 + C_3 T_{er}^2 + C_4 T_{er} T_{cr} + C_5 \omega_r^2 T_{er} + C_6 T_{cr}^2 \omega_r^2$$

Table 6: Coefficients for efficiency correlations

B_0	4.1890229	C_1	0.472016327
B_1	1.24550014	C_2	-23.4915664
B_2	-1.65814515	C_3	-23.2113301
B_3	0.851259913	C_4	46.3226046
B_4	-0.788119616	C_5	-0.524246134
C_0	0.744036625	C_6	0.348140304

with

$T_{cr} = T_c[\mathrm{K}]/(353.13\ \mathrm{K})$

$T_{er} = T_e[\mathrm{K}]/(313.15\ \mathrm{K})$

$\omega_r = \omega[\mathrm{rad \cdot s^{-1}}]/(345.575\ \mathrm{rad \cdot s^{-1}})$

5. INTEGRATED ANALYSIS

5.1 General Results

During the course of an orbit, the satellite will be exposed to a wide range of effective surrounding temperatures, and the variation in ambient temperature will consequently impact the working temperatures of the system. Figure 6 shows the results for the system performance for two ambient temperatures of 220 K and 130 K for fixed capacity and displacement per revolution of the compressor. At T_∞ = 220 K, as the rotational speed of the compressor increases, the evaporating temperature decreases and the condensing temperature increases. The increase in temperature lift results in a monotonic decrease in COP with rotational speed. When the ambient temperature decreases, the evaporating and condensing pressures also decrease (as does their difference), and as a result, the COP of the system at a T_∞ of 130 K is better than that of the system at a T_∞ of 220 K.

The two most important parameters are the COP of the system and the temperatures of the electrical components. From a consideration of the COP, the slower the rotational speed, the better. The optimal rotational speed is that which yields exactly the required component temperatures as this rotational speed will maximize the COP.

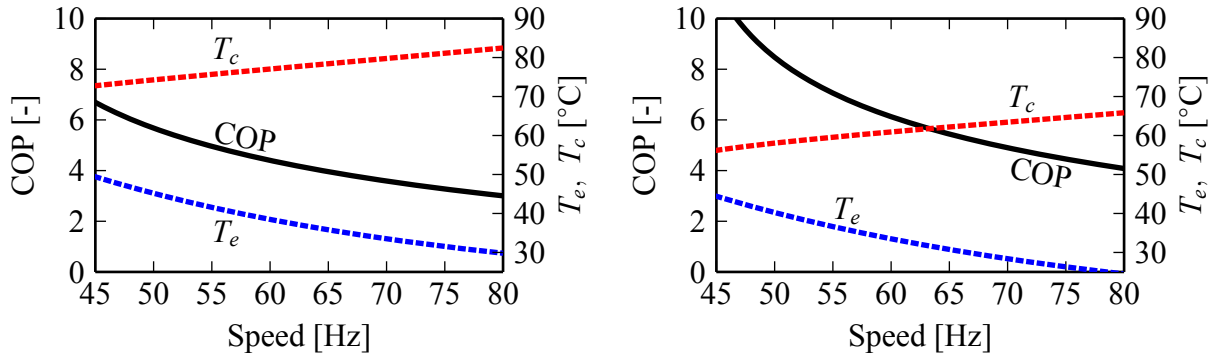

(a) Overall results at T_∞ = 220 K

(b) Overall results at T_∞ = 130 K

Figure 6: Overall results for two different effective surroundings temperatures as a function of compressor rotational speed (A_{rad} = 25 m^2, V_{disp} = 45 cm^3·rev^{-1})

5.2 Detailed Results

The remaining analysis will focus on one operational point in detail in order to investigate the performance of the heat exchangers, compressor, and demonstrate some features of the system. The most important values are summarized in Table 7. To begin with, Figure 7(a) shows the temperature profiles in the condenser. Here we see the three zones in the heat exchanger, first a de-superheating zone, then a two-phase zone, and finally the subcooled zone. The surface temperature of the radiator is much more strongly tied to the fluid temperature than the ambient temperature. Thus we can say that the limiting thermal resistance is that between the radiator surface temperature T_s and the ambient temperature T_∞.

Figure 7(b) shows the temperature profiles in the evaporator. The refrigerant temperature decreases in the two-phase region (by approximately 1.5 K) due to the impact of the pressure drop (total pressure drop is around 40 kPa), while the refrigerant temperature increases in the superheated zone. The surface (component) temperature increases near the end of the evaporator due to the strong decrease in heat transfer coefficient caused by dryout in the transition from two-phase to superheated vapor, as shown in Figure 7(c). The high component temperatures in the dryout zone are a significant cause for concern, as there are few electronic components that could handle a component temperature of 150°C. Thus the flux applied to the evaporator should be decreased in the dryout zone of the evaporator.

Table 7: Output parameters for selected point

Parameter	Value	Parameter	Value	Parameter	Value	Parameter	Value
T_e	38.5°C	T_c	77.1°C	COP	4.40	$\dot{m}$	58.7 g/s
Δp_{rad}	65.0 kPa	Δp_{evap}	36.1 kPa	η_{oi}	0.665	η_v	0.818

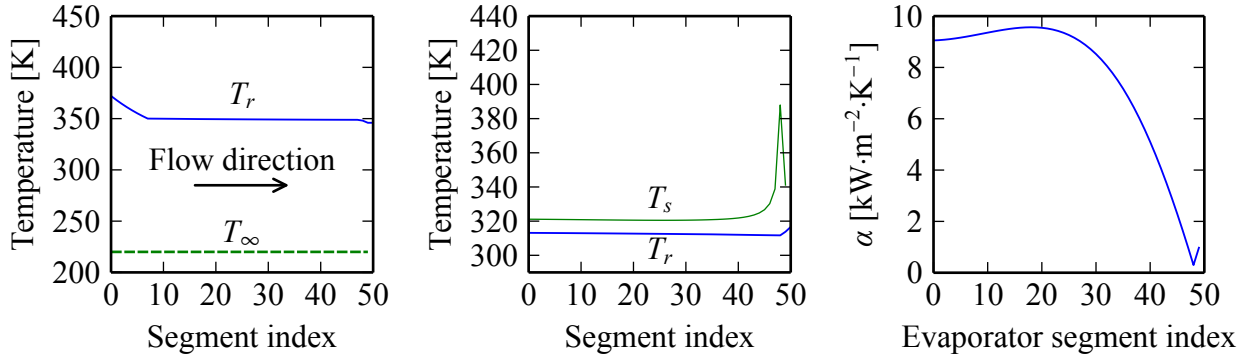

(a) Temperatures in the radiator (b) Temperatures in the evaporator (c) Heat transfer coefficient in the evaporator

Figure 7: Detailed analysis (A_{rad} = 25 m^2, T_∞ = 220 K, V_{disp} = 45 cm^3·rev^{-1}, f = 60 Hz)

CONCLUSIONS

The following conclusions can be obtained from this study:

- The refrigerant R152A is found to be a good working fluid for this system due to its high efficiency and reasonable compressor sizing
- The COP that can be achieved are quite good (> 4 for reasonable conditions), thanks to the good compressor efficiency as predicted by PDSim
- The component temperatures in the evaporator are quite high in the refrigerant dryout region - when designing satellite heat pump systems (and electronic cooling systems in general), it is critical to have sufficient factor of safety on the thermal design in the dryout and superheated zones

NOMENCLATURE

A_{rad}	Radiator area (m^2)
h_i	Internal height of channel (m)
L_{rad}	Length of the radiator (m)
$L_{circuit}$	Length of the circuit (m)
$\dot{m}$	Mass flow rate ($kg \cdot s^{-1}$)
N_{pass}	Number of passes (-)
q'	Heat transfer per unit length ($W \cdot m^{-1}$)
q''	Heat transfer per area ($W \cdot m^{-2}$)
R_{conv}	Convective thermal resistance ($m^2 \cdot K \cdot W^{-1}$)
R_{total}	Total thermal resistance ($m^2 \cdot K \cdot W^{-1}$)
R_{TIM}	Thermal interface resistance ($m^2 \cdot K \cdot W^{-1}$)
T_c	Cond. saturated temperature (K)
T_{cr}	Reduced cond. sat. temp (-)
T_{crit}	Critical temperature (K)
T_e	Evap. saturated temperature (K)
T_{er}	Reduced evap. sat. temp (-)
T_s	Cond. surface temperature (K)
T_r	Cond. refrigerant temperature (K)
T_{triple}	Triple point temperature (K)
ΔT_{sh}	Compressor inlet superheat (K)
α	Heat transfer coefficient ($W \cdot m^{-2} \cdot K^{-1}$)
ω	Rotational speed ($rad \cdot s^{-1}$)
ω_r	Reduced rotational speed (-)
η_0	Overall surface effectiveness (-)
η_{oi}	Overall isentropic efficiency (-)
η_v	Volumetric efficiency (-)
COP	Coeff. of Performance (-)
w_i	Internal width of channel (m)
w_{mc}	Width of microchannel condenser (m)
w_{pass}	Width of radiator pass (m)
ε	Radiator emissivity (-)

REFERENCES

Bell, I. H., Wronski, J., Quoilin, S., and Lemort, V. (2014). Pure and Pseudo-pure Fluid Thermophysical Property Evaluation and the Open-Source Thermophysical Property Library CoolProp. *Industrial & Engineering Chemistry Research*, 53(6):2498--2508.

Bertsch, S. S., Groll, E. A., and Garimella, S. V. (2009). A composite heat transfer correlation for saturated flow boiling in small channels. *International Journal of Heat and Mass Transfer*, 52:2110--2118.

Churchill, S. (1977). Friction factor equation spans all fluid flow regimes. *Chemical Engineering*, 84(24):91--92.

Gnielinski, V. (1975). Neue Gleichungen für den Wärme-und den Stoffübergang in turbulent durchströmten Rohren und Kanälen. *Forschung im Ingenieurwesen*, 41(1):8--16.

Herwig, H. (2013). High Heat Flux Cooling of Electronics: The Need for a Paradigm Shift. *Journal of Heat Transfer*, 135:111013--1:2.

Kim, S.-M. and Mudawar, I. (2012). Universal approach to predicting two-phase frictional pressure drop for adiabatic and condensing mini/micro-channel flows. *International Journal of Heat and Mass Transfer*, 55:3246--3261.

Kim, S.-M. and Mudawar, I. (2013). Universal approach to predicting two-phase frictional pressure drop for mini/micro-channel saturated flow boiling. *International Journal of Heat and Mass Transfer*, 58:718--734.

Shah, M. (1979). A general correlation for heat transfer during film condensation inside pipes. *International Journal of Heat and Mass Transfer*, 22:547--556.